Influence of strain rate and phase history on the spall failure of single and polycrystal tin

Jasper G. Threadingham,[1] Xuefei Liang,[1] Edward Leggett,[1] Liam Smith,[1] Jeremy C. F. Millett,[2] Glenn Whiteman,[2] Viviane Peçanha-Antonio,[3] Andrew T. Boothroyd,[3] David J. Chapman,[1] and Daniel E. Eakins[1]
[1]*Department of Engineering Science, University of Oxford, Oxford, OX1 3PJ, UK*
[2]*AWE, Aldermaston, Reading, RG7 4PR, UK*
[3]*Department of Physics, University of Oxford, Oxford, OX1 3PU, UK*

(*Electronic mail: daniel.eakins@eng.ox.ac.uk)

(Dated: 27 May 2026)

Spall occurs when materials are subjected to shock impacts; under this loading, the material properties can be modified through microstructural changes and phase transitions. The effect of these changes on subsequent spall has been underexplored. The anisotropy of tin's ambient crystal structure and the accessibility of the $\beta \rightarrow \gamma$ solid-solid phase transition under shock loading means that tin offers a rich domain in which to study spall failure. Through testing single-crystal and polycrystal samples shocked above and below this transition, the effects of these variables on the deformation behaviour of tin can be determined. Although no orientation dependent spall behaviour is observed, unusual strain-rate-dependent behaviour is observed, indicating likely mechanisms for the high-rate behaviour of tin.

I. INTRODUCTION

When compressive shock waves reflect from surfaces, tensile waves can be created. The interaction of such waves can result in the creation of new surfaces through internal tensile failure, commonly known as spall. The phenomenon of spall is not a fixed material property, but rather a dynamic response shaped by a number of factors of both the experiment and the sample. In particular, the role of microstructure[1–4], crystal orientation[1,5–8], release strain-rate[9–11], phase transformations[12] and peak shock pressure[10,13–15] can all influence the mechanisms of spall.

One particularly interesting feature of tin is the asymmetry of its ambient phase, β-tin[16,17]. This phase takes the form of a diamond lattice compressed along the diagonal, resulting in properties such as the electrical resistivity[18], yield strength[19], thermal expansion[18,20–24] and compressibility[18,25–30] all showing a clear dependence on the orientation of the crystal. Tin also undergoes a phase transition to a tetragonal γ phase at approximately 9 GPa under shock loading[31]. This phase transformation is readily accessible under shock, and is associated with a significant refinement of the grain size[32–34]. Together these phenomena mean tin offers a rich domain of states in which to test spall failure. Through testing spall in a range of single- and polycrystal samples, both above and below this phase transition, a better understanding of the underlying behaviours of tin can also be reached, complementing the authors' previous study of the Hugoniot states of single crystal tin[31].

A. Background

The earliest spall measurements of tin by Lalle in Grady[10] map the drop in spall strength corresponding to melt-on-release, with the dataset later expanded by Kanel *et al.*[13]. Between these two sources, measurements are mainly between a peak pressure of 15 and 30 GPa. These data were later augmented with additional experiments and modelling by Robert *et al.*[15] and most recently by Wu *et al.*[35]. The damage induced in these two key loading situations, namely solid and melt on release, has also been studied using proton radiography[36].

Together, these show a strong drop in spall strength as the peak shock pressure increases, see Figure 4. However, some uncertainty remains regarding the strength of the solid phases. Some authors have suggested that spall strength may increase slightly with peak pressure[35], although there is considerable variation between sources.

While these studies all use peak shock pressure to heat the sample, a number of studies preheat or cool the sample to investigate the spall strength. In one such example by Zaretsky and Kanel[14], the sample's initial temperature is varied, showing a very weak decrease in spall strength for temperatures below ambient, and a very rapid drop off approaching the melt point. With peak free-surface velocities around $400\,\mathrm{m\,s^{-1}}$, the material is unlikely to reach stresses high enough to induce the transition to the γ phase and the time at low temperatures insufficient for significant α to form. Similarly Kanel *et al.*[37] and Ashitkov *et al.*[38] preheat the sample prior to spall to test the strength of the liquid phase.

Spall has also been observed using ramp wave loading, with Chong *et al.*[39] using this loading to measure the spall strength in samples that have reached the γ phase. Laser driven shocks have also been used to measure the spall strength of solid tin. Moshe *et al.*[9] investigate the spall strength and its relationship with the spall strain-rate. The quoted particle velocities for these experiments are in the range $0.29\,\mathrm{km\,s^{-1}}$ to $0.8\,\mathrm{km\,s^{-1}}$, indicating a range of peak pressures spanning the β and γ phases. However, neither the particle velocity nor pressure is published, meaning the pressure history cannot be estimated.

Combined with recovery, laser driven shocks have been used to investigate the onset of melting upon release[40–43]. Fielding velocimetry at low pressures shows a clear pull-back corresponding to spall, while at higher pressures no such clear pull-back is visible. Indeed the increased noise levels are perhaps a better indication of the change in phase than the numerical values attributed to the pull-back for the high-pressure tests. Considering also the large decay in peak shock-pressure between the driven and free surfaces, these results perhaps bridge between the domain of spall and the domain of dynamic fragmentation. The use of X-rays to diagnose the phase and temperature of the fragments released and modelling by Yang *et al.*[44] adds additional data underlining the complexity of this loading case.

Spall in tin has been modelled, most notably using molecular dynamics in single crystals[45–48]. With molecular dynamics being able to model the underlying phenomenon, such as the initiation, growth and coalescence of voids, these computational studies offer insights beyond that which can be achieved by free-surface measurements, or even X-ray imaging[49]. However, it remains to be seen how closely these simulations match experimental values, highlighting the need for experimental measurements.

As such, reliable and accurate measurements are required to isolate the influence of strain-rate, peak-pressure and phase on the spall behaviour. The influence of single crystal orientation is also an important consideration. Given anisotropic spall behaviour has been found in materials with greater crystal symmetry than tin such as molybdenum[5], copper[6,7] and aluminium[1,8], studying the spall in single crystal tin is imperative to better understand the orientation dependent behaviour of the material. Spall is also dependent on the microstructure[1–3], so studying spall above and below the β to γ phase transition may indicate any changes in the microstructure that occur.

II. METHODS

Continuing the experiments the authors presented in[31], a 'top-hat' geometry, Figure 1, is used. This design, using a C101 copper driver plate upon which photon Doppler velocimetry (PDV) is fielded using the double telecentric array[50], allows for the shock wave speeds to be measured, and also provides a datum from which the crystal orientation can be quantified. With a scope sampling rate of $40\,\mathrm{GS\,s^{-1}}$, a typical window size of 128 samples and a 50 % overlap are used, giving a time resolution of 1.6 ns. Where the PDV signal is weaker, the window size is increased to 256 samples, corresponding to a resolution of 3.2 ns. While this geometry is optimised for Hugoniot measurements, characteristic pull-backs are present in the free-surface traces, allowing analysis of spall in single-crystal tin above and below the phase transition.

Tests using this setup are conducted at four impact velocities, on three single-crystal orientations (001), (100), and (110), and polycrystal samples. The single crystals are all of diameter 10 mm and were indexed relative to the driver plate in order to compare the shock tilt to the crystal axis; see Figure 1. Polycrystal samples were cut from a stock bar with a diameter of 11 mm. All sample densities were determined using the Archimedes method. The sample thickness was measured before and after mounting, although the depth gauge used was unable to resolve the difference in thickness, meaning the glue layer is assumed to be less than the resolution of 0.01 mm. Sample measurements, including Hugoniot state measurements are presented in Appendix A.

Two tests are conducted with peak pressures above the threshold for the β to γ phase transition and two below. Thus, comparison between the spall strength of material that has undergone a transition and that which has not in single-crystal and polycrystal samples can be made. In addition, further polycrystal tests are conducted using different thickness samples and flyers to study the strain-rate dependence of spall. Experimental data are tabulated in Table II, and selected rear surface traces are presented in Figure 2.

Experimental traces are linearly segmented to analytically determine the pull-back height; see Figure 3. Not only does this approach simplify the inherently noisy PDV signals, but it also allows bridging of the regions where the signal drops out. The velocity prior to pull-back u_{max} and the lowest velocity reached u_{min} are then calculated from the intersections between the fits. Given the peak state is assumed to be constant, the uncertainty of u_{max} is estimated using the 95 % confidence interval of the fit to the peak state. Similarly, the uncertainty of u_{min} is estimated to be the 95 % confidence interval of the pull-back fit evaluated at the minimum point.

To determine the optimum fit, a brute force optimisation is applied. The peak state is determined through minimising the free-surface uncertainty (see[31] for additional details), while the pull-back is determined through minimising the uncertainty of both u_{max} and u_{min}.

A. Spall strength

The simplest method of determining the spall strength uses the drop in the free-surface velocity (Δu, the difference between u_{max} and u_{min}), to estimate the corresponding tensile stress at failure σ using

$$\sigma = \frac{1}{2}\rho_0 c \Delta u. \tag{1}$$

Here, ρ_0 denotes the initial density of the tin sample and c the wave speed. This wave speed is typically taken as the bulk sound speed, representing a wave speed slower than the initial release wave from the rear free surface, and the ambient elastic wave speed; but above the shear wave speed.

This equation is used extensively in the polycrystal tin spall literature. For instance, Robert *et al.*[15] use equation 1 with a sound speed of $2.8\,\mathrm{km\,s^{-1}}$, corresponding with the bulk sound speed calculated from the polycrystal wave speeds of Marsh[52]. The same equation is used by Kanel *et al.*[13], although the wave speed used is not specified. De Rességuier *et al.* also use the bulk sound speed to evaluate equation 1 without giving a value[40–43]. Wu *et al.*[35] use a value of $2.61\,\mathrm{km\,s^{-1}}$, in contrast to the other studies. This corresponds with the value of C used by that source to fit the Hugoniot of tin using a linear $U_{\mathrm{s}} - u_{\mathrm{p}}$ relationship, equation 7. Due to the $\beta \rightarrow \gamma$ phase transition, the equation does not well model the low pressure phase, acting to average the discontinuity in properties across the transition. Accounting for the transition using the multiphase Birch-Murnaghan model proposed by Mabire[53,54]

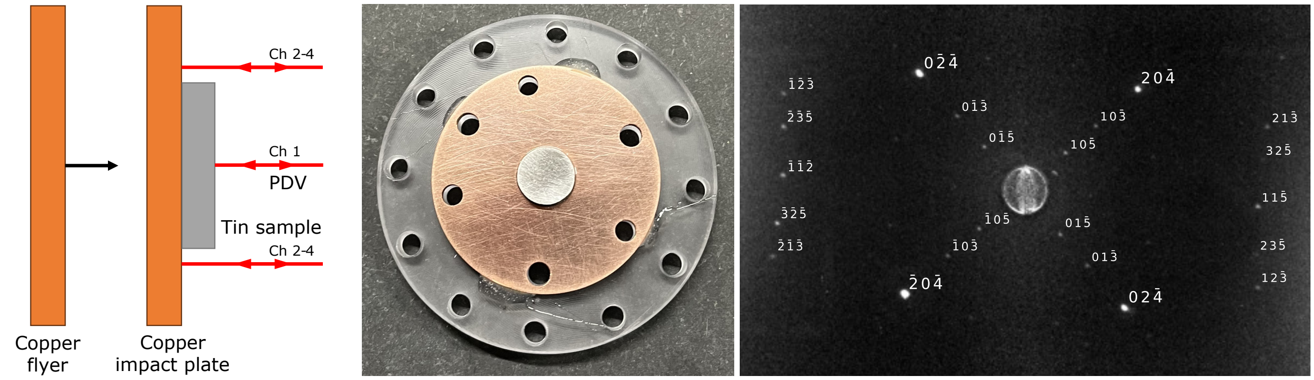

(a) Schematic representation of the plate impact experiments. PDV measures the rear surface of the tin sample and the copper driver plate.

(b) Image of a target mounted onto a driver plate and support ring. The pattern of holes on the copper plate has no rotational symmetry, providing a datum for shock tilt and crystal rotation measurements.

(c) Diffraction pattern for sample 001_1 with diffraction spots labelled.

FIG. 1: Target geometry used in plate-impact experiments. A driver disk with no rotational symmetry is used to index the crystal and measure the shock front tilt. PDV is fielded to measure the surface velocities and transmission speeds. Reproduced from Threadingham *et al.*[31], "Effects of crystal orientation on the shock properties of single crystal tin," © Crown Owned Copyright 2025/AWE, and is reused here under the same copyright

yields an ambient $C = 2.75\,\mathrm{km\,s^{-1}}$. Considering the consistent use throughout the literature, and proximity to the zero pressure wave speed from this multi-phase model, a polycrystal bulk sound speed of $2.8\,\mathrm{km\,s^{-1}}$ is used in this study. The data from Wu *et al.*[35] have been adjusted in Figures 4 and 5 to account for this methodological difference. Spall studies in liquid tin, meanwhile, uses a liquid sound speed typically of between $2.2\,\mathrm{km\,s^{-1}}$ to $2.5\,\mathrm{km\,s^{-1}}$[37,38,55].

In single-crystal samples with orientation dependent properties, the wave speed used to calculate spall strength requires careful consideration. In different orientations, single crystals often exhibit different properties, particularly compressibilities and wave speeds. A consensus has not yet emerged regarding the sound speed to use for single-crystal spall, with, for example, Chen *et al.*[1] using the polycrystal sound speed to determine the spall strength of single-crystal aluminium, while Owen *et al.*[8] calculate the bulk sound speed for the specific orientations of aluminium single-crystals tested, going as far as to calculate two strengths for orientations where two shear waves can propagate.

In β tin, with its tetragonal structure, the wave speeds vary more than in higher symmetry materials, and two shear sound speeds can be determined for the principal directions. Ambient single-crystal wave speeds are tabulated in Table I, with estimations of bulk sound speeds for each mode. While the bulk sound speeds for (001) align well with the literature polycrystal value, (100) shows a significantly slower longitudinal sound speed and corresponding bulk sound speeds. Orientation (110) shows the most unusual behaviour, with one shear sound speed almost a factor of two lower than for other systems. As a result, applying equation 1 with the most divergent speeds for each orientation would result in spall strengths that vary by up to 30 %.

However, under shock loading, a number of processes act to change the crystal properties, meaning the ambient wave speeds may not be the most appropriate. It has been noted, for instance, that grain size is significantly refined when tin is shocked,[32–34], suggesting that single-crystals likely devolve into polycrystals. The polycrystal sound speeds[52], $c_\mathrm{b} = 2.8\,\mathrm{km\,s^{-1}}$ and $c_\mathrm{l} = 3.43\,\mathrm{km\,s^{-1}}$ are used in this work for polycrystal and single-crystal samples, with further discussion of the appropriateness of these values presented in III.

B. Correction for spall plate thickness

During spall, the wave-front of the recompression wave typically over-takes part of the tensile wave, resulting in a reduced pull-back magnitude on the free surface. This can be corrected by adapting equation 1 using

$$\sigma = \frac{1}{2}\rho_0 c_\mathrm{b}\left(\Delta u_\mathrm{fs} + \delta\right). \tag{2}$$

All symbols have their usual meanings, and δ, the correction, can be found through

$$\delta = \left(\frac{h}{c_\mathrm{b}} - \frac{h}{c_\mathrm{l}}\right)\frac{|\dot{u}_1 \dot{u}_2|}{|\dot{u}_1| + \dot{u}_2}, \tag{3}$$

where $\dot{u}_1$ and $\dot{u}_2$ are the slope of the pull-back and rebound respectively, c_l the longitudinal wave speed, c_b the bulk wave speed and h is the depth of the spall plane[57–59].

Given the lack of symmetry in the impact geometry, the spall depth thickness must be estimated from the velocimetry traces, for which there are two principle methods[57]. First, the primary release can be used. Assuming the release from the

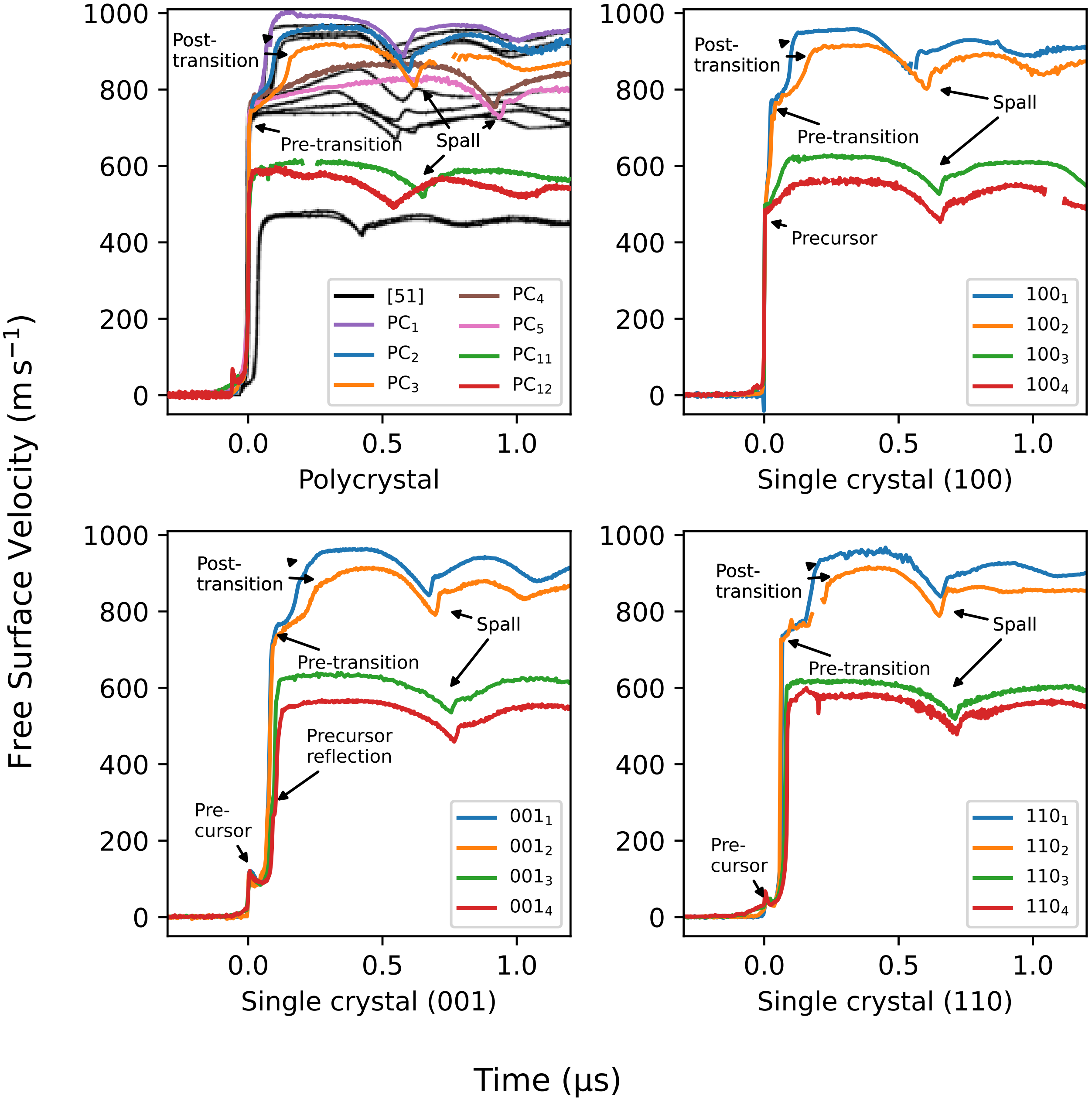

FIG. 2: Surface velocities traces indicate spall failure in the tin samples. The polycrystal data of Anderson *et al.*[51] (black lines), reproduced from W. W. Anderson *et al.*, “Phase transition and spall behavior in β-tin,” in Shock Compression of Condensed Matter - 1999 (AIP Publishing, 2000) pp. 443–446, with the permission of AIP Publishing, is plotted for comparison, applying a linear dispersion correction to account for the different sample thickness.

TABLE I: Table of sound speeds for each single-crystal orientation. All speeds are in units of km s^{-1}.

	Primary Orientation		Secondary direction 1			Secondary direction 2	
	Longitudinal sound speed[56]		Shear sound speed[56]	Bulk sound speed		Shear sound speed[56]	Bulk sound speed
(001)	3.446 ± 0.015	(110)	1.727 ± 0.008	2.810 ± 0.026	(010)	1.718 ± 0.007	2.819 ± 0.025
	3.430 ± 0.010			2.791 ± 0.019			2.799 ± 0.019
(100)	3.112 ± 0.015	(001)	1.717 ± 0.008	2.399 ± 0.028	(010)	1.795 ± 0.008	2.321 ± 0.029
(110)	3.481 ± 0.018	(001)	1.739 ± 0.010	2.843 ± 0.028	$(1\bar{1}0)$	0.955 ± 0.005	3.302 ± 0.029

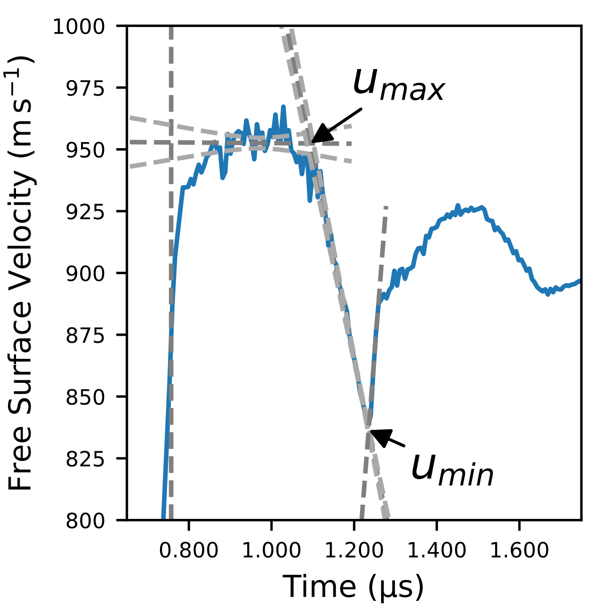

FIG. 3: Linear fits (dark grey lines) are taken to determine the peak state, the pull-back and the rebound. Intersections between these lines are then calculated to determine the maximum and minimum velocities. Light grey lines show 95 % confidence intervals.

measured free surface travels to the spall plane with a velocity c_b, while the re-compression wave travels with velocity c_l, the spall depth h is given by

$$h = t_{\text{spall}} \frac{c_b c_l}{c_b + c_l}. \tag{4}$$

The time t_{spall} is taken from the difference between the incident wave's arrival on the free-surface and the arrival time of the minimum (u_{min}). For (100), the precursor is the largest forward wave and is therefore used to define t_{spall}, Figure 2, while for all other orientations, the pre-transition wave is used.

Alternatively, the secondary reflections of the release and compression from the spall surface can be used. This approach uses the period of the ringing after the shock recompression t_{ringing} to estimate the spall depth. This assumes that the trapped reverberation waves travel with the longitudinal wave-speed c_l, giving

$$h = \frac{1}{2} t_{\text{ringing}} (c_l). \tag{5}$$

In these experiments, equation 4 offers the most robust method, with spall reverberations often showing dispersion, noisy velocimetry signals and dropouts. Fitting a sinusoid to estimate either the second minimum or period of the reverberations offers a method to overcome some of these shortcomings, however, the fit is often poorly conditioned. In addition, the period of the reverberations tends to decrease with further periods, where available, suggesting a degree of damping. As a result, only equation 4 is used when calculating the spall strength in equation 3, although both are presented in Table II.

C. Spall strain-rate

Typically, the strain rate of spall ($\dot{\varepsilon}$) is given as

$$\dot{\varepsilon} \approx \frac{\Delta u}{\Delta t} \frac{1}{2c_b}. \tag{6}$$

Here, $\frac{\Delta u}{\Delta t}$ is taken as the gradient of the linear fit to the pull-back (the line between u_{max} and u_{min} in Figure 3). This is fitted to the developed release wave immediately prior to the inflection and therefore corresponds to the local conditions at the nucleation of damage. Defining Δt from the start of roll-off would, therefore, underestimate the strain rate for the specific conditions where spall first occurs. To the author's knowledge, this equation first occurs in English speaking literature in Kanel *et al.*[58]. Prior to this, the pressure-rate was used in a similar manner, with pressure measured using a transducer on the rear surface instead of velocity measurements[60–62]. Earlier sources use only the pulse width[63,64] to assess the onset of spall failure. Intermediate derivations may lie in Russian literature sources.

This equation relies on several key assumptions. First, it is assumed that spall initiates immediately after the final release from the sample free surface, meaning only the release wave from the flyer drives the nucleation and growth of spall. Second, the release wave is assumed to disperse minimally, with the release strain-rate being constant throughout the sample. Finally, the material is assumed to display a linear pressure-volume relationship, meaning wave interactions are additive. As a consequence of these assumptions, the free-surface strain rate calculated through equation 6 can be taken as a proxy for the strain rate on the spall plane. This provides a useful estimate for the strain rate, and has been used to determine the threshold between ductile and brittle behaviour[9,10,50].

It has been noted that the spall strain rate calculated by this equation systematically underestimates the strain rate when compared to computational simulations[65]. Indeed, it is suggested by Utkin[66] that the strain rate on the measured surface calculated through equation 6 is one quarter the strain rate at the spall plane. An alternative analysis by Antoun *et al.*[57] yields the same conclusion.

The assumption of negligible dispersion of the release wave is also possibly unreliable, with plate-impact experiments typically represented with a release fan, the release from the flyer dispersing approximately linearly. Many material's Hugoniots are modelled using the relationship

$$U_s = C + S u_p, \tag{7}$$

where U_s is the wave velocity, C and S constants and u_p the particle velocity[52,67]. While the release follows an isentrope, for low pressures, the release follows the Hugoniot to within a few percent, and equation 7 provides a reasonable estimate,[68]. From this, the pull-back, itself a decrease in u_p with time, would correspond with a linear decrease in the wave velocity as u_p decreases, creating a release fan originating temporally from a single time on the flyer free-surface. This of course neglects any disturbance caused by the interaction of the two releases from opposing surfaces. However, in this case, the strain rates vary through the sample by a factor α relative to the strain-rate at the measured-surface, where

$$\alpha = \frac{y_0}{y_0 - y}. \tag{8}$$

Here, y is the distance from the measured free-surface, and y_0 is the thickness of the sample and flyer, with a full derivation in Appendix B. If y is taken as h, the depth of the spall plane from the measured surface, then the spall strain rate is given by

$$\dot{\varepsilon}_\mathrm{corrected} \approx 4\alpha \frac{\Delta u}{\Delta t}\frac{1}{2c_\mathrm{b}} = \frac{y_0}{y_0 - h}\frac{\Delta u}{\Delta t}\frac{2}{c_\mathrm{b}}. \tag{9}$$

This equation remains valid where spall first occurs on the final release wavelet from the measured free surface. Thus the initiation of spall is driven by release from the flyer. For this to be true, h must be less than half y_0.

For classical spall experiments, where the impactor is thinner than, and of the same material as, the sample, this simple approximation may significantly improve the accuracy of the spall strain rate measurement. For instance, in the case of Turley *et al.*[65], experimental measurements of strain rate determined by equation 6 differed from strain rates calculated in simulations by a factor of six. In this case the samples are twice as thick as the flyer ($y_0 = 3, h = 1$) meaning a correcting factor of $\alpha = 3/2$ should be applied. Through the application of equation 9, the reported factor of six difference between simulated strain rates and measured values is thereby accounted for.

III. RESULTS

A qualitative analysis of these traces indicates that the spall pull-back profiles are very similar for the various orientations. The samples all show a similar sharp rise, followed by a plateau leading to a more gradual rise indicative of a transition from a faster rate of damage to a slower rate, typically assumed to be the transition from brittle to ductile behaviour[69]. This effect is also present in the traces of Anderson *et al.*[51]. It is noted that Anderson *et al.* use thicker samples. To compare the traces with the work conducted here in Figure 2, a linear scaling factor is applied to the time axis to account for the different sample thickness. Despite this, the thicker samples have the effect of softening and dispersing the sharp kick.

The similarity between orientations is borne out in the measured spall strengths. Using equation 1 with the bulk sound speed of $2.8\,\mathrm{km\,s^{-1}}$ gives the results presented in Figure 4. The use of a single sound speed for all orientations allows for a comparison of the magnitude of the pull-back between samples, and between the literature and these experiments. Preliminary data, based on the release waves arrival on the copper and tin free-surfaces, indicate that the release wave speeds are similar between samples. Some clear trends are visible from this analysis.

First, no clear distinction between single crystals and polycrystals can be made. This is somewhat unexpected: typically, a grain structure is expected to reduce the spall strength. For example, molybdenum and copper single crystals show spall strengths roughly twice as high as polycrystals[5–7], while aluminium offers a roughly 20 % difference[1,8]. Given also that the experimental traces show an almost identical pull-back profile, with similar rebound characteristics, orientation does not appear to influence spall. As a result, the use of a single wave speed is perhaps the more appropriate approach.

A further observation is made that samples that have undergone the γ phase change appear to show a somewhat higher pull-back magnitude than those that have not, although the explanation of this behaviour is unclear.

A. Strain rate

The spall strengths presented here sit somewhat higher than the gas-gun and explosively driven experiments of Lalle in Grady[10], Kanel *et al.*[13] and Robert *et al.*[15], but below the laser driven measurements of de Rességuier *et al.*[42] in Figure 4. Given the associated strain rate of these experimental methods, it is suggested that the strain rate may strongly influence the spall strength of tin. In literature spall strain rate measurements, equation 6 is used[9]. For other literature studies, the strain-rate can be estimated from the presented velocity traces. In most studies, experimental geometries are not documented, meaning equation 9 cannot be applied. In order to compare results, equation 6 must be used, with results in Figure 5.

Estimating the spall strain-rate confirms that the data presented here sit at higher strain rates than other literature gas-gun data. The experimental geometry for the literature data is not published, meaning variations in sample and flyer thickness may explain the difference between these data and the literature.

Inspecting Figure 5, the data follow a straight line, with the exception of the two highest polycrystal data points. As a result, it may be that the jump in spall strength observed in Figure 4 for material that has cycled $\beta \to \gamma \to \beta$ is an effect of the strain rate rather than any change in properties resulting from the phase changes. A change in spall strength due to the phase history would be expected to result in different trends for samples that had undergone the transition and those that had not. These phenomena are not observed in the data with all data agreeing with the straight line fits. The higher rate experiments meanwhile do not show any increase in spall strength. This behaviour is typically assumed to be indicative of a brittle to ductile transition, following the theory proposed by Grady[10].

The ductile spall strength, where fracture is dominated by energy dissipated through plastic yielding, can be determined

TABLE II: Table of spall data

Sample	Peak	Pull-back	Pull-back gradient	Spall strength	Spall strain-rate	Spall depth		Corrected	Corrected Spall
	state	magnitude				Primary[a]	Secondary[b]	spall strength	strain-rate
	phase	$\mathrm{m\,s^{-1}}$	$\times 10^8 \mathrm{m/s^2}$	GPa	$\times 10^5$	mm	mm	GPa	$\times 10^5/\mathrm{s}$
100_1	γ	117 ± 2	6.9 ± 0.2	1.19 ± 0.03	1.24 ± 0.03	0.82	0.76	1.47	5.81 ± 0.15
100_2	γ	116 ± 8	7.4 ± 0.7	1.18 ± 0.09	1.32 ± 0.12	0.89	0.79	1.50	6.26 ± 0.57
100_3	β	94 ± 4	5.7 ± 0.3	0.96 ± 0.05	1.02 ± 0.05	0.92	1.09	1.25	4.87 ± 0.24
100_4	β	103 ± 10	6.8 ± 0.7	1.05 ± 0.10	1.21 ± 0.12	0.91	0.94	1.34	5.79 ± 0.58
001_1	γ	128 ± 3	8.6 ± 0.3	1.31 ± 0.03	1.53 ± 0.05	0.94	0.70	1.75	7.34 ± 0.24
001_2	γ	128 ± 3	8.4 ± 0.2	1.30 ± 0.04	1.51 ± 0.04	0.98	0.59	1.78	7.31 ± 0.20
001_3	β	94 ± 5	5.3 ± 0.4	0.96 ± 0.05	0.94 ± 0.06	1.01	1.11	1.21	4.60 ± 0.30
001_4	β	101 ± 5	5.4 ± 0.4	1.03 ± 0.05	0.97 ± 0.07	1.03	1.10	1.34	4.74 ± 0.35
110_1	γ	116 ± 6	8.2 ± 0.6	1.18 ± 0.07	1.47 ± 0.10	0.92	0.75	1.55	7.01 ± 0.48
110_2	γ	130 ± 5	9.7 ± 0.5	1.33 ± 0.06	1.74 ± 0.08	0.92	0.42	1.78	8.31 ± 0.39
110_3	β	87 ± 5	5.4 ± 0.5	0.88 ± 0.06	0.96 ± 0.08	0.98	1.13	1.17	4.67 ± 0.39
110_4	β	99 ± 9	6.3 ± 1.2	1.01 ± 0.09	1.12 ± 0.20	0.98	1.09	1.31	5.45 ± 0.98
PC_1	γ	111 ± 28	8.3 ± 0.4	1.13 ± 0.29	1.48 ± 0.06	0.90	0.72	1.49	7.09 ± 0.29
PC_2	γ	119 ± 8	7.6 ± 0.6	1.21 ± 0.08	1.36 ± 0.11	0.93	0.70	1.61	6.58 ± 0.54
PC_3	γ	116 ± 9	10.8 ± 1.1	1.19 ± 0.09	1.93 ± 0.20	0.96	0.74	1.68	9.47 ± 0.99
PC_4	γ	120 ± 4	8.0 ± 0.4	1.23 ± 0.05	1.43 ± 0.07	1.42	1.10	1.79	7.59 ± 0.38
PC_5	β and γ mix	107 ± 5	6.5 ± 0.4	1.09 ± 0.05	1.16 ± 0.06	1.45	0.87	1.60	6.19 ± 0.33
PC_6	γ	113 ± 4	9.1 ± 0.5	1.15 ± 0.04	1.62 ± 0.08	1.25	1.01	1.66	8.11 ± 0.41
PC_8	γ	122 ± 3	8.8 ± 0.2	1.24 ± 0.03	1.57 ± 0.02	0.58	0.46	1.53	7.14 ± 0.10
PC_9	γ	113 ± 6	8.7 ± 0.7	1.16 ± 0.07	1.56 ± 0.12	1.34	1.02	1.77	8.06 ± 0.62
PC_{10}	γ	109 ± 12	11.3 ± 1.5	1.11 ± 0.12	2.01 ± 0.26	0.54	0.49	1.43	8.90 ± 1.16
PC_{11}	β	86 ± 4	5.4 ± 0.4	0.88 ± 0.05	0.96 ± 0.06	1.01	0.88	1.14	4.75 ± 0.30
PC_{12}	β	95 ± 9	4.6 ± 0.2	0.96 ± 0.10	0.82 ± 0.04	0.84	0.82	1.10	3.91 ± 0.20

[a] Spall depth calculated from the reflection of the first release wave from the free surface, equation 4.

[b] Spall depth calculated from the secondary reflection of the release, i.e. the first reverberation after spall, equation 5.

using

$$\sigma = (2\rho c^2 Y \varepsilon_c)^{\frac{1}{2}} \tag{10}$$

where Y is the flow stress in simple tension, given by Grady as a range between 0.05 and 0.12 GPa for tin, while ε_c is the critical void volume fraction, taken as 0.15. Taking the middle of the range of Y as 0.085 GPa, the density as $7290\,\mathrm{kg\,m^{-3}}$ and the bulk sound speed c as $2.8\,\mathrm{km\,s^{-1}}$ yields a value of 1.2 GPa. This is in good agreement with the highest spall strengths measured in these experiments, as well as the laser shocks of Moshe *et al.*[9] and de Rességuier *et al.*[40–43]. The post-spall recovered samples of de Rességuier *et al.* confirm that ductile fracture, predominantly trans-granular, is the mechanism of spall in this domain[41].

After applying the spall strength and strain-rate corrections, it can be seen by visually inspecting Figure 6b that the highest strain-rate tests, assumed to fail through ductile spall, show a spall strength around 1.75 GPa. This is in better agreement with the data from de Rességuier *et al.*[40–43] than Moshe *et al.*[9], see Figure 5, although neither apply the correction for spall depth (equation 3). However, with pulse durations of approximately 10 ns, more than an order of magnitude shorter than the pulse here, the correction would likely be a similar magnitude smaller, and therefore not significantly change the values.

Below this, the rate-dependent region is assumed to be governed by rate-dependent cracking. For many structural materials, such as aluminium, uranium, molybdenum, beryllium and steel[5,10,11,70,71], this phenomenon can be modelled assuming energy dissipation through the creation of new surfaces. In this case

$$\sigma = (3\rho c K_c^2 \dot{\varepsilon})^{\frac{1}{3}} \tag{11}$$

gives the spall strength, where K_c is the fracture toughness of the material[10]. However, for many other materials, applying a more general fit of the form

$$\sigma = a\dot{\varepsilon}^n \tag{12}$$

better maps the spall strength. Many common metals exhibit a power n to be less than $\frac{1}{3}$, with stainless steel 35Kh3NM, titanium, copper and magnesium Mg95, exhibiting n to be in the range of 0.05 to 0.25.[1,57] This may be due to the variation of K_c with strain rate: fracture toughness typically decreases with strain rate as the reduced time duration decreases energy dissipation through plastic work[72].

A least squares fit conducted on the data for tin measured in this study, excluding the two highest polycrystal data points (samples PC_3 and PC_{10}), yields an unusually high power of $n = 0.509$,(three decimal places, variance of 0.004). Including the literature data from Robert *et al.*[15], Chong *et al.*[39], Kanel *et al.*[13] Holtkamp *et al.*[36], and the data for Wu *et al.*[35] with a peak pressure below 13 GPa, into the fit yields $n = 0.481$ (variance of 0.002). Correcting the strain rate and the spall strength only increases the power (Figure 6b), further deviating from the brittle model.

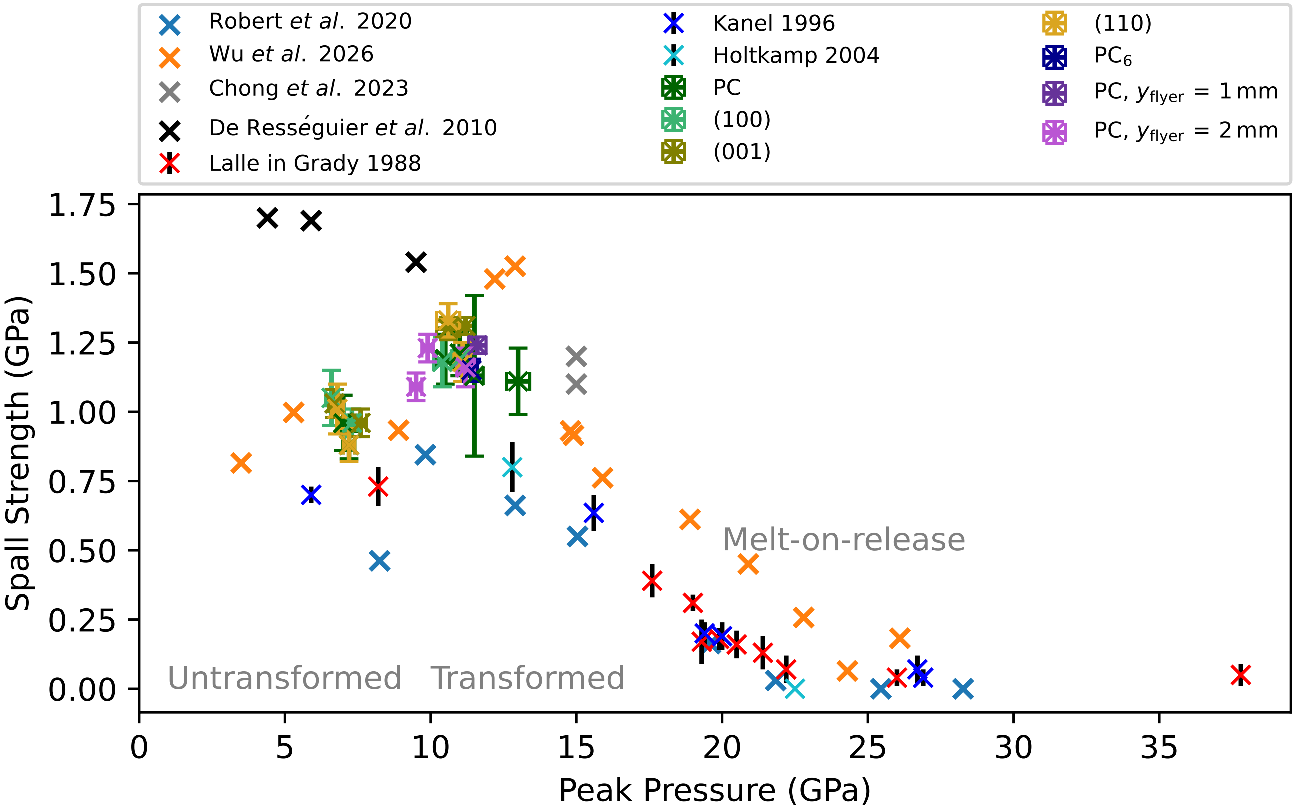

FIG. 4: Uncorrected spall strengths presented for a range of single and polycrystal samples of tin. Using a bulk sound speed of $2.8\,\mathrm{km\,s^{-1}}$ for all samples allows for comparison of the pull-back magnitude between the literature[10,13,15,35,36,39,42] and the various samples. All samples use a 1.5 mm thick copper flyer (y_{flyer}) and are nominally 2 mm thick unless otherwise stated, except for sample PC_6, ($y_{\mathrm{flyer}} = 2\,\mathrm{mm}$, $y_0 = 3\,\mathrm{mm}$). Labels used to indicate approximate regions where the samples remain β (untransformed), undergo the forward and reverse transition to γ (transformed) and melt prior to spall failure.

Limited evidence in tin-based solders suggests that fracture toughness increases with strain rate[73], although the transferability to pure tin and the strain rates measured under shock is unclear. The authors are aware of no measurements of the fracture toughness of pure tin beyond soldered joints[74]. However, if K_c were a function of strain rate, equation 11 would still hold, and could map to a higher power than one third. Indeed, any strain rate relationship would have to approximate $K_c \propto \dot{\varepsilon}^{0.25}$ for equation 11 to map to a power of a half. This would imply that tin had no resistance to cracking when the strain rate is equal to zero. Any offset of the form $K_c = a\dot{\varepsilon}^{\frac{1}{4}} + b$, where a and b are constants would result in a non-linearity in $\log\dot{\varepsilon}$ - $\log\sigma$ space (Figure 5). However, no curvature is visible in the data presented, although further testing in the lower strain-rate domain would improve the confidence in this assessment.

Taken together, this behaviour suggests that tin may not conform to traditional brittle fracture models, but instead exhibits characteristics more consistent with a material governed by viscous dissipation mechanisms. Notably a power law relationship of

$$\sigma = (2\rho c^2 \eta \dot{\varepsilon})^{\frac{1}{2}} \tag{13}$$

is predicted for a material where viscous dissipation dominates the spall strength[10].

Given the spall strength is around three orders of magnitude larger than the statically observed critically resolved shear stresses[19,75–77], it is supposed that plastic deformation is readily facilitated, forming the dominant deformation mechanism during the nucleation and growth of voids. Therefore, the spall behaviour could be governed by the energy dissipation during this plastic flow, rather than through surface energy in brittle fracture. Tin is also known for exhibiting creep deformation[78–85] at low strain rates. With forces used to induce creep in the mega-pascal domain and quasi-static strain rates, extrapolation to the shock domain is unable to offer any meaningful results. Nonetheless, the observed power-law rate-dependence of spall could point to similar underlying mechanisms, meaning creep behaviour could offer a window to interpreting the viscous-like response of tin at high strain rates.

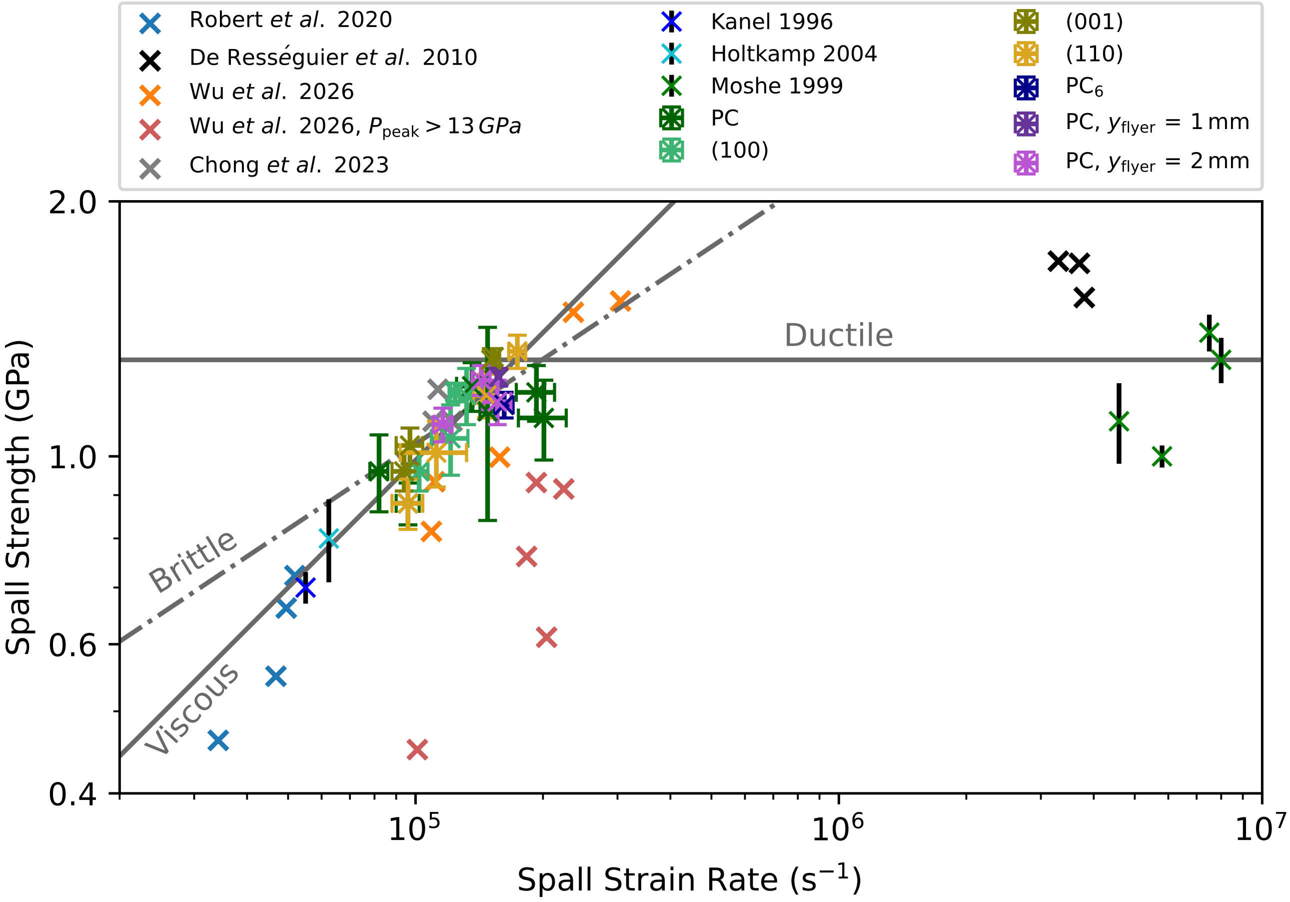

FIG. 5: Spall strain-rate and strength for a range of tin samples and peak pressures compared to the literature[9,13,15,35,36,39,42]. A bulk sound speed of 2.8 $\mathrm{km\,s^{-1}}$ is used to estimate the spall strength and strain rate. Grey dotted line used as a guide between samples in this study that transforms to the γ phase at the peak state. All samples use a 1.5 mm thick copper flyer (y_{flyer}) and are nominally 2 mm thick unless otherwise indicated, except for sample PC_6, ($y_{\mathrm{flyer}} = 2$ mm, $y_0 = 3$ mm).

A viscous-like flow could well explain other observations of the high-pressure behaviour of tin such as the lack of observed anisotropy above the elastic-plastic transition under shock[31]. Once the viscous flow regime is activated, initial orientation and texture may no longer be preserved to any great extent. Similarly, this flow like structure would be unable to preserve any changes induced by the phase transition cycle, meaning spall is limited by the flow regardless of the phase history. However, the order-of-magnitude difference of the elastic limit between the orientations remains a puzzle, especially given the lack of a clear Schmidt law response[31].

Further recovery and *in situ* X-ray experiments are, therefore, required to better understand the mechanism of spall in tin. Additionally, molecular dynamics studies may help develop understanding on the phenomenon through predictions of the atomic scale processes involved.

B. Further observations

Examining Figure 6a highlights the need to apply the correction for the spall strain rate, equation 9. Samples impacted with a thicker flyer appear to show a higher spall strength for the same strain rate, while those impacted with a thinner flyer show lower spall strength. No reason beyond analytical inaccuracies is thought to be behind this effect. Indeed, after applying the correction (equation 9 with y_0 taken as the total thickness of the flyer, driver plate and sample to produce Figure 6b), this spread is no longer observed. The samples impacted with 2 mm and 1 mm flyers now sit much closer to the trend-line. The proposed correction can, therefore, reduce at least some of the error inherent in the assumptions used to derive equation 6, despite the different materials used in the flyer and driver plate.

However, the data points still sit towards the edges of the trend-line. For the experiments presented here, the linear

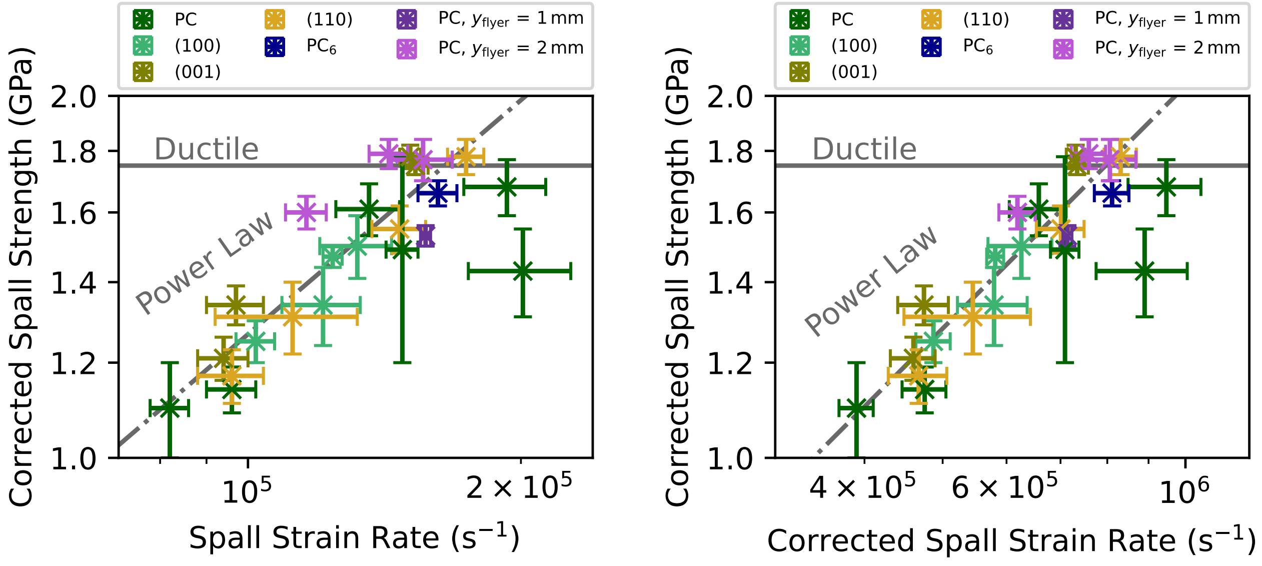

(a)

(b)

FIG. 6: Spall strengths, corrected for re-compression overtake (equations 2 and 3), compared to the uncorrected strain rate (equation 6, left) and strain-rate corrected for dispersion (equation 9, right). Samples are impacted with a 1.5 mm flyer (y_{flyer}) and are 2 mm thick, unless otherwise noted, except for PC$_6$, which uses a 2 mm flyer and 3 mm sample.

approximation gives a much more empirical estimate of the strain rate, given equation 9 assumes that dispersion is linear. The dispersion rates in the copper driver and tin sample will be different, while the impedance mismatch between the two adds additional complexity. Two approaches could be taken to account for this. Following an approach similar to the derivation of the spall strength equation, the dispersion rates could be approximated using the ratio c_l to c_b for the two materials. The coupling between the two could then be estimated using the elastic moduli to convert the strain rate on one side of the interface to the other, based on stress and displacement continuity. An alternative approach, assuming predominantly plastic deformation, would be to use pressure-particle-velocity matching. Assuming a relationship given by equation 7, the gradient S could be used to give a measure of the dispersion in the two materials, with the shock jump conditions used to estimate the coupling. However, it is unclear without further analysis and modelling, such as through hydrocode simulations, whether either of these two approaches would yield a better result for the experimental geometry tested here. In particular, neither approach would model well the distortion in the profile caused by the γ to β phase transition, nor the interactions between the various waves.

The use of these additional corrections relies heavily on the validity of the underlying assumptions regarding material behaviour. Since each assumption may deviate from a more accurate representation, such as one obtained through hydrocode modelling, reducing the number of assumptions may lead to a more robust model. Applying additional corrections based on dispersion rates without additional modelling would, therefore, complicate the simplicity of equation 9, without necessarily improving the accuracy. As such, applying equation 9 in Figure 6 with the uncertainty from equation 6 scaled appropriately appears to significantly reduce scatter from the expected trend. For a classical spall experiment, where the flyer and sample are of the material, equation 9 is expected to have the best results.

Applying the corrections highlights that the highest pressure polycrystal (PC$_{10}$) sits detached from the main trend. It may be the case that sample is starting to weaken with the onset of melt. In Figure 4, the transition between solid spall and liquid spall shows a decrease in spall strength. The lower end of this transition region is not clearly defined, but appears to be around 12 GPa to 15 GPa, in which region this sample is shocked.

IV. CONCLUSIONS

In this study, the effects of spall strain-rate, single crystal orientation and peak phase on the spall strength of tin have been examined. Any anticipated orientation or microstructural dependence of the spall strength, based on the static properties and comparison to other materials, is not found in tin. Instead, the spall strength of solid tin appears to be best predicted using only the strain rate. The nature of this strain-rate dependence appears to correlate with a viscous model, with spall strength proportional to the square root of strain-rate. This response, it is hypothesised, may be due to the low threshold for plastic deformation resulting in fluid-like flow. This hypothesis may help the understanding of other shock observations, such as the lack of any observed orientation dependence of the Hugoniot states above the Hugoniot elastic limit, with the plastic flow overcoming any pre-shock properties. An improvement to the calculation of the spall strain rate for plate-impact experiments is also proposed. To better verify these observations, further experimental measurements are suggested alongside additional modelling. Key areas of focus could include molecular dynamics simulations of shock and spall in tin, alongside *in situ* X-ray diagnostics of phase and microstructure, or shock recovery.

V. ACKNOWLEDGEMENTS

The authors gratefully acknowledge AWE for their continued support. Thanks also to Stuart Carter and the ISML workshop for their help manufacturing samples and consumables. Thanks to Martí Puig Fantauzzi for valuable conversations regarding molecular dynamics models of tin. UK Ministry of Defence © Crown Owned Copyright 2025/AWE.

VI. AUTHOR DECLARATIONS

A. Conflicts of Interest

The authors have no conflicts to disclose.

B. Author Contributions

Jasper G. Threadingham: Conceptualisation (lead); Data curation (lead); Formal analysis (lead); Investigation (lead); Methodology (lead); Writing – original draft (lead); Writing – review & editing (lead). **Xuefei Liang**: Investigation (equal). **Edward Leggett**: Investigation (equal); Writing – review & editing (equal). **Liam C. Smith**: Investigation (equal); Writing – review & editing (equal). **Jeremy C. F. Millett**: Conceptualisation (supporting); Funding acquisition (equal) Resources (equal); Supervision (supporting). **Glenn Whiteman**: Conceptualisation (supporting); Funding acquisition (equal); Resources (equal); Supervision (supporting). **Viviane Peçanha-Antonio**: Methodology (supporting); Resources (supporting). **Andrew T. Boothroyd**: Methodology (supporting); Resources (supporting); Writing – review & editing (supporting). **David J. Chapman**: Conceptualisation (equal); Funding acquisition (equal); Investigation (equal); Supervision (equal); Writing – review & editing (equal). **Daniel E. Eakins**: Conceptualisation (equal); Funding acquisition (lead); Investigation (equal); Supervision (lead); Writing – review & editing (equal).

C. Data Availability

The data that support the findings of this study are available from the corresponding author upon reasonable request.

Appendix A: Shock wave data

Measured pressures and shock wave speeds are presented in Table III alongside the sample data.

Appendix B: Derivation of equation 8

Assuming a simple wave with momentum and mass conservation, wave propagation is given by

$$\frac{\partial u_\mathrm{p}}{\partial t} + U_\mathrm{s}(u_\mathrm{p})\frac{\partial u_\mathrm{p}}{\partial y} = 0. \tag{B1}$$

If U_s can be estimated given u_p by equation 7, a step change from $u_{\mathrm{p}0}$ to $u_{\mathrm{p}1}$ at $t=0$ and $y=0$ results in u_p varying in space and time by

$$u_\mathrm{p}(y,t) = \begin{cases} u_{\mathrm{p}0}, & y < (C+Su_{\mathrm{p}0})t \\ \frac{y-Ct}{St}, & (C+Su_{\mathrm{p}1})t < y < (C+Su_{\mathrm{p}0})t \\ u_{\mathrm{p}1}, & y > (C+Su_{\mathrm{p}1})t \end{cases}. \tag{B2}$$

In the decreasing region

$$\frac{\partial u_\mathrm{p}}{\partial t} = \frac{-y}{St^2}. \tag{B3}$$

Evaluated along a line of constant u_p,

$$\left.\frac{\partial u_\mathrm{p}}{\partial t}(y)\right|_{t=y/(C+Su_\mathrm{p})} = \frac{-(C+Su_\mathrm{p})^2}{Sy} \propto \frac{1}{y}. \tag{B4}$$

Notably, this neglects any change in u_p due to the opposing release fans interacting. However, the ratio at a given point y to the surface is given by

$$\alpha = \frac{\frac{\partial u_\mathrm{p}}{\partial t}(y_0-y)}{\frac{\partial u_\mathrm{p}}{\partial t}(y_0)} = \frac{y_0}{y_0-y}. \tag{B5}$$

Appendix C: References

[1] X. Chen, J. R. Asay, S. K. Dwivedi, and D. P. Field, "Spall behavior of aluminum with varying microstructures," Journal of Applied Physics **99** (2006), 10.1063/1.2165409.

[2] D. A. Dalton, D. L. Worthington, P. A. Sherek, N. A. Pedrazas, H. J. Quevedo, A. C. Bernstein, P. Rambo, J. Schwarz, A. Edens, M. Geissel, I. C. Smith, E. M. Taleff, and T. Ditmire, "Microstructure dependence of dynamic fracture and yielding in aluminum and an aluminum alloy at strain rates of $2\times10^6\,\mathrm{s}^{-1}$ and faster," Journal of Applied Physics **110** (2011), 10.1063/1.3660214.

TABLE III: Table of experimental and sample data.

Sample	Impact Velocity ($\mathrm{m\,s^{-1}}$)	Thickness y_0 (mm)	Shock Tilt[a]		Crystal Rotation[b]				Precursor		
			Angle (mrad)	Rotation (rad)	R_x (mrad)	R_y (mrad)	R_z (mrad)	C_l ($\mathrm{m\,s^{-1}}$)	u_p ($\mathrm{m\,s^{-1}}$)	σ (GPa)	V/V_0
100_1[c]	775 ± 2	2.08 ± 0.01	5.0 ± 0.3	2.60 ± 0.07	−3 ± 2	871 ± 2	−3 ± 2	3.31 ± 0.04	225 ± 11	5.4 ± 0.4	0.932 ± 0.005
100_2[c]	742 ± 1	2.08 ± 0.01	6.4 ± 0.5	−2.66 ± 0.07	3 ± 2	−1216 ± 2	−2 ± 2	3.31 ± 0.04	217 ± 8	5.2 ± 0.3	0.934 ± 0.003
100_3	519 ± 1	2.19 ± 0.01	2.5 ± 0.2	−0.57 ± 0.07	4 ± 2	865 ± 2	15 ± 2	3.30 ± 0.03	248 ± 3	6.0 ± 0.2	0.925 ± 0.002
100_4	470 ± 1	2.12 ± 0.01	5.1 ± 0.2	2.31 ± 0.03	4 ± 2	192 ± 2	2 ± 2	3.29 ± 0.03	236 ± 7	5.7 ± 0.3	0.928 ± 0.003
001_1[c]	777 ± 1	2.10 ± 0.01	0.3 ± 0.2	−0.84 ± 0.67	5 ± 2	717 ± 2	−5 ± 2	3.71 ± 0.04	61 ± 4	1.7 ± 0.2	0.984 ± 0.002
001_2[c]	743 ± 3	2.06 ± 0.01	4.5 ± 0.3	−3.06 ± 0.04	−9 ± 2	−236 ± 2	−7 ± 2	3.74 ± 0.05	58 ± 6	1.6 ± 0.2	0.984 ± 0.002
001_3	529 ± 1	2.09 ± 0.01	5.5 ± 0.2	−0.43 ± 0.04	1 ± 2	438 ± 2	9 ± 2	3.75 ± 0.07	62 ± 2	1.7 ± 0.1	0.983 ± 0.001
001_4	472 ± 1	2.04 ± 0.01	0.4 ± 0.2	−2.36 ± 0.35	8 ± 2	406 ± 2	9 ± 2	3.72 ± 0.03	56 ± 2	1.5 ± 0.1	0.985 ± 0.001
110_1[c]	765 ± 2	2.15 ± 0.01	5.2 ± 0.4	1.31 ± 0.05	0 ± 2	665 ± 2	0 ± 2	3.70 ± 0.06	24 ± 6	0.7 ± 0.2	0.993 ± 0.002
110_2[c]	742 ± 2	2.12 ± 0.01	8.2 ± 0.5	−2.77 ± 0.06	3 ± 2	−1466 ± 2	−2 ± 2	3.63 ± 0.08	26 ± 7	0.7 ± 0.2	0.993 ± 0.002
110_3	513 ± 1	2.04 ± 0.01	5.8 ± 0.2	2.90 ± 0.04	7 ± 2	−1388 ± 2	4 ± 2	3.60 ± 0.03	26 ± 2	0.7 ± 0.1	0.993 ± 0.001
110_4	485 ± 2	2.04 ± 0.01	7.4 ± 0.3	−2.82 ± 0.09	−1 ± 2	−861 ± 2	6 ± 2	3.66 ± 0.04	37 ± 4	1.0 ± 0.2	0.990 ± 0.002
PC_1[c]	809 ± 2	1.92 ± 0.01	2.2 ± 0.2	-	-	-	-	3.45 ± 0.03	19 ± 2	0.5 ± 0.1	0.994 ± 0.001
PC_2[c]	776 ± 1	1.96 ± 0.01	7.0 ± 0.5	-	-	-	-	3.46 ± 0.03	24 ± 5	0.6 ± 0.2	0.993 ± 0.002
PC_3[c]	746 ± 2	1.85 ± 0.01	6.5 ± 0.3	-	-	-	-	3.50 ± 0.07	20 ± 5	0.5 ± 0.2	0.994 ± 0.002
PC_4[c]	711 ± 2	1.75 ± 0.01	2.1 ± 0.3	-	-	-	-	3.44 ± 0.04	31 ± 6	0.8 ± 0.2	0.991 ± 0.002
PC_5[c]	646 ± 2	1.84 ± 0.01	1.1 ± 0.4	-	-	-	-	3.65 ± 0.11	17 ± 5	0.5 ± 0.2	0.995 ± 0.002
PC_6[c]	785 ± 3	2.81 ± 0.01	3.1 ± 0.3	-	-	-	-	3.52 ± 0.03	15 ± 4	0.4 ± 0.1	0.996 ± 0.002
PC_7[cd]	782 ± 1	1.00 ± 0.01	5.0 ± 0.4	-	-	-	-	3.52 ± 0.06	37 ± 2	0.9 ± 0.1	0.990 ± 0.001
PC_8[c]	786 ± 1	1.87 ± 0.01	5.5 ± 0.4	-	-	-	-	3.61 ± 0.05	20 ± 3	0.5 ± 0.1	0.995 ± 0.001
PC_9[c]	770 ± 5	1.96 ± 0.01	6.0 ± 0.5	-	-	-	-	3.64 ± 0.05	23 ± 10	0.6 ± 0.3	0.994 ± 0.003
PC_{10}[e]	878 ± 9	2.02 ± 0.01	3.3 ± 0.4	-	-	-	-	3.56 ± 0.06	26 ± 2	0.7 ± 0.1	0.993 ± 0.001
PC_{11}	504 ± 1	1.75 ± 0.01	1.4 ± 0.2	-	-	-	-	3.48 ± 0.04	25 ± 6	0.6 ± 0.2	0.993 ± 0.002
PC_{12}	477 ± 3	1.78 ± 0.01	7.1 ± 0.3	-	-	-	-	3.58 ± 0.04	35 ± 5	0.9 ± 0.2	0.990 ± 0.002

Sample	Density	Pre-transition				Post-transition			
	ρ_0 ($\mathrm{g\,cm^{-3}}$)	U_s ($\mathrm{km\,s^{-1}}$)	u_p ($\mathrm{m\,s^{-1}}$)	P (GPa)	V/V_0	U_s ($\mathrm{km\,s^{-1}}$)	u_p ($\mathrm{m\,s^{-1}}$)	P (GPa)	V/V_0
100_1[c]	7.28 ± 0.02	3.22 ± 0.04	380 ± 3	9.0 ± 0.2	0.884 ± 0.003	2.97 ± 0.05	474 ± 1	11.0 ± 0.2	0.852 ± 0.003
100_2[c]	7.28 ± 0.02	3.18 ± 0.04	376 ± 6	8.9 ± 0.3	0.884 ± 0.003	2.79 ± 0.06	453 ± 2	10.4 ± 0.3	0.856 ± 0.003
100_3	7.29 ± 0.02	3.06 ± 0.07	310 ± 1	7.3 ± 0.2	0.905 ± 0.002	-	-	-	-
100_4	7.29 ± 0.02	3.02 ± 0.09	279 ± 3	6.6 ± 0.2	0.914 ± 0.002	-	-	-	-
001_1[c]	7.28 ± 0.02	3.26 ± 0.04	377 ± 2	9.1 ± 0.2	0.886 ± 0.002	2.91 ± 0.11	477 ± 1	11.2 ± 0.3	0.851 ± 0.003
001_2[c]	7.28 ± 0.02	3.26 ± 0.05	361 ± 2	8.8 ± 0.3	0.892 ± 0.003	2.74 ± 0.20	454 ± 2	10.6 ± 0.4	0.857 ± 0.005
001_3	7.29 ± 0.02	3.21 ± 0.05	317 ± 2	7.6 ± 0.2	0.904 ± 0.002	-	-	-	-
001_4	7.29 ± 0.02	3.14 ± 0.04	281 ± 1	6.7 ± 0.2	0.913 ± 0.002	-	-	-	-
110_1[c]	7.28 ± 0.02	3.35 ± 0.06	367 ± 2	9.0 ± 0.3	0.891 ± 0.003	2.97 ± 0.05	463 ± 2	11.1 ± 0.3	0.858 ± 0.003
110_2[c]	7.29 ± 0.02	3.30 ± 0.07	361 ± 5	8.8 ± 0.4	0.891 ± 0.004	2.77 ± 0.11	454 ± 3	10.6 ± 0.4	0.857 ± 0.005
110_3	7.29 ± 0.02	3.18 ± 0.03	309 ± 1	7.2 ± 0.2	0.904 ± 0.002	-	-	-	-
110_4	7.29 ± 0.02	3.19 ± 0.04	287 ± 2	6.8 ± 0.2	0.911 ± 0.002	-	-	-	-
PC_1[c]	7.29 ± 0.02	3.24 ± 0.03	369 ± 4	8.8 ± 0.2	0.886 ± 0.003	2.99 ± 0.08	496 ± 1	11.5 ± 0.3	0.844 ± 0.003
PC_2[c]	7.29 ± 0.02	3.26 ± 0.03	378 ± 3	9.0 ± 0.2	0.884 ± 0.002	2.92 ± 0.06	473 ± 2	11.0 ± 0.2	0.851 ± 0.003
PC_3[c]	7.28 ± 0.02	3.27 ± 0.06	364 ± 2	8.7 ± 0.3	0.889 ± 0.003	2.72 ± 0.07	456 ± 2	10.5 ± 0.3	0.854 ± 0.004
PC_4[c]	7.28 ± 0.02	3.25 ± 0.04	387 ± 1	9.2 ± 0.2	0.881 ± 0.002	2.39 ± 0.05	429 ± 1	9.9 ± 0.2	0.863 ± 0.003
PC_5[cf]	7.29 ± 0.02	3.26 ± 0.04	380 ± 1	9.1 ± 0.2	0.884 ± 0.002	2.15 ± 0.09	411 ± 1	9.5 ± 0.2	0.868 ± 0.003
PC_6[c]	7.29 ± 0.01	3.34 ± 0.02	378 ± 2	9.2 ± 0.1	0.887 ± 0.001	3.00 ± 0.06	478 ± 1	11.4 ± 0.2	0.853 ± 0.002
PC_7[cd]	7.29 ± 0.02	3.28 ± 0.06	384 ± 2	9.2 ± 0.3	0.884 ± 0.003	2.89 ± 0.08	478 ± 1	11.2 ± 0.3	0.850 ± 0.004
PC_8[c]	7.29 ± 0.02	3.36 ± 0.04	374 ± 2	9.2 ± 0.2	0.889 ± 0.002	3.00 ± 0.07	483 ± 2	11.6 ± 0.3	0.852 ± 0.003
PC_9[c]	7.29 ± 0.02	3.36 ± 0.04	385 ± 3	9.5 ± 0.3	0.886 ± 0.003	2.98 ± 0.06	466 ± 2	11.2 ± 0.3	0.858 ± 0.003
PC_{10}[e]	7.29 ± 0.02	3.32 ± 0.04	390 ± 99	9.5 ± 2.6	0.883 ± 0.031	3.29 ± 0.06	536 ± 7	13.0 ± 0.4	0.839 ± 0.005
PC_{11}	7.28 ± 0.02	3.23 ± 0.04	304 ± 1	7.2 ± 0.2	0.906 ± 0.002	-	-	-	-
PC_{12}	7.28 ± 0.02	3.19 ± 0.04	295 ± 1	7.0 ± 0.2	0.909 ± 0.002	-	-	-	-

[a] Shock tilt angle is given by the angle between the normal of the shock plane and the normal of the driver plate (y axis). The rotation is given as the rotation of the normal of the shock plane projected onto the driver plate, positive taken as clockwise from the vertical (z axis), defined by the mirror symmetry of the target (see Figure 1b)

[b] Crystal rotation is given as the angle of the specified orientation relative to the normal to the driver plate (y axis). The x axis is horizontal, while the z axis is the vertical axis formed by the mirror symmetry (see Figure 1b).

[c] This data was initially presented in Threadingham *et al.*[31], "Effects of crystal orientation on the shock properties of single crystal tin," © Crown Owned Copyright 2025/AWE, and is reused here under the same copyright.

[d] With a 2 mm thick flyer and 1 mm thick sample, typical spall behaviour is not observed in this sample.

[e] Experiment initially presented in[50] and reanalysed in[31].

[f] Phase transition incomplete. Post transition state taken as highest state reached before spall.

[3] N. A. Pedrazas, D. L. Worthington, D. A. Dalton, P. A. Sherek, S. P. Steuck, H. J. Quevedo, A. C. Bernstein, E. M. Taleff, and T. Ditmire, "Effects of microstructure and composition on spall fracture in aluminum," Materials Science and Engineering: A **536**, 117–123 (2012).

[4] T. P. Remington, E. N. Hahn, S. Zhao, R. Flanagan, J. C. Mertens, S. Sabbaghianrad, T. G. Langdon, C. E. Wehrenberg, B. R. Maddox, D. C. Swift, B. A. Remington, N. Chawla, and M. A. Meyers, "Spall strength dependence on grain size and strain rate in tantalum," Acta Materialia **158**, 313–329 (2018).

[5] G. I. Kanel, S. V. Razorenov, A. V. Utkin, V. E. Fortov, K. Baumung, H. U. Karow, D. Rusch, and V. Licht, "Spall strength of molybdenum single crystals," Journal of Applied Physics **74**, 7162–7165 (1993).

[6] S. V. Razorenov, E. B. Zaretsky, and A. S. Savinykh, "The spall strength and Hugoniot elastic limit of mono-crystalline and polycrystalline copper near melting temperature," in *18th APS-SCCM and 24th AIRAPT*, Vol. 500 (Institute of Physics Publishing, 2014).

[7] S. V. Razorenov, A. S. Savinykh, and E. B. Zaretsky, "Elastic-plastic deformation and fracture of shock-compressed single-crystal and polycrystalline copper near melting," Technical Physics **58**, 1437–1442 (2013).

[8] G. D. Owen, D. J. Chapman, G. Whiteman, S. M. Stirk, J. C. Millett, and S. Johnson, "Spall behaviour of single crystal aluminium at three principal orientations," Journal of Applied Physics **122** (2017), 10.1063/1.4999559.

[9] E. Moshe, S. Eliezer, E. Dekel, Z. Henis, A. Ludmirsky, I. B. Goldberg, and D. Eliezer, "Measurements of laser driven spallation in tin and zinc using an optical recording velocity interferometer system," Journal of Applied Physics **86**, 4242–4248 (1999).

[10] D. E. Grady, "The spall strength of condensed matter," Journal of the Mechanics and Physics of Solids **36**, 353–384 (1988).

[11] J. Buchar, S. Rolc, and J. Hrebícek, "Strain rate dependence of the spall strength of steels," Journal de Physique IV **7** (1997), 10.1051/jp4:19973160.

[12] M. A. Meyers and C. T. Aimone, "Dynamic fracture (spalling) of metals," Progress in Materials Science **28**, 1–96 (1983).

[13] G. I. Kanel, S. V. Razorenov, A. V. Utkin, and D. E. Grady, "The spall strength of metals at elevated temperatures," in *Shock Compression of Condensed Matter-1995* (AIP Publishing, 1996) pp. 503–506.

[14] Zaretsky, E. B. and Kanel, G. I., "Dynamic response of sn over the temperature range 115–503 k," DYMAT - International Conference on the Mechanical and Physical Behaviour of Materials under Dynamic Loading **1**, 27–33 (2009).

[15] G. Robert, L. Pillon, G. Seisson, and C. Chauvin, "Full multiphase description of materials: Application on tin," in *Shock Compression of Condensed Matter-2019*, Vol. 2272 (American Institute of Physics Inc., 2020).

[16] H. Mark and M. Polanyi, "Die gitterstruktur, gleitrichtungen und gleitebenen des weißen zinns," Zeitschrift für Physik **18**, 75–96 (1923).

[17] H. Mark and M. Polanyi, "Zur gitterstruktur des weißien zinns," Zeitschrift für Physik **22**, 200 (1924).

[18] P. W. Bridgman, "Some properties of single metal crystals," Proceedings of the National Academy of Sciences **10** (1924).

[19] G. I. Kirichenko, "Anisotropy of plastic deformation of tin single crystals in the temperature range 4.2-300K," The Physics of Metals and Metallography **63**, 144–151 (1987).

[20] V. T. Deshpande and D. B. Sirdesmukh, "Thermal expansion of tetragonal tin," Acta Crystallographica **14**, 355–356 (1961).

[21] C. B. G. and S. Weintroub, "The measurement of the thermal expansion of single crystals of tin by an interferometric method," Proceedings of the Physical Society. Section B **63**, 267–277 (1950).

[22] M. Straumanis and A. Ievinš, "Die bestimmung von ausdehnungskoeffizienten nach der pulver- und der drehkristall-methode," Zeitschrift für anorganische und allgemeine Chemie **238**, 175–188 (1938).

[23] G. F. Kossolapow and A. K. Trapesnikow, "Struktubericht Band IV," (Akademische Verlagsgesellschaft M.B.H. Leipzig, 1936) Chap. Zinn, Sn: Röntgenographische Bestimmung der thermischen Ausdehnungskoeffizienten von Beryllium und Zinn. Z. Kristallogr. (A) 94 (1936) 53-59, p. 88.

[24] G. Shinoda, "X-ray investigations on the thermal expansions of solids," Memoirs of the College of Science, Kyoto Imperial University, Series A **16**, 193–201 (1933).

[25] S. C. Prasad and W. A. Wooster, "The study of the elastic constants of white tin by diffuse X-ray reflexion," Acta Crystallographica **8**, 682–686 (1955).

[26] W. P. Mason and H. E. Bommel, "Ultrasonic attenuation at low temperatures for metals in the normal and superconducting states," Journal of the Acoustical Society of America **28**, 930–943 (1956).

[27] D. G. House and E. V. Vernon, "Determination of the elastic moduli of tin single crystals, and their variation with temperature," British Journal of Applied Physics **11**, 254 (1960).

[28] J. A. Rayne and B. S. Chandrasekhar, "Elastic constants of β tin from 4.2°k to 300°k," Physical Review **120**, 1658–1663 (1960).

[29] L. C. Cardinal, "Report of NRL progress, March 1963," (U. S. Naval Research Laboratory, 1963) Chap. Vibro Analysis of Material, pp. 31–32.

[30] E. W. Kammer, L. C. Cardinal, C. L. Vold, and M. E. Glicksman, "The elastic constants for single-crystal bismuth and tin from room temperature to the melting point," Journal of Physics and Chemistry of Solids **33**, 1891–1892 (1972).

[31] J. G. Threadingham, X. Liang, E. Leggett, L. C. Smith, J. C. F. Millett, G. Whiteman, V. Peçanha-Antonio, A. T. Boothroyd, D. J. Chapman, and D. E. Eakins, "Effects of crystal orientation on the shock properties of single crystal tin," Journal of Applied Physics (2025), Under review.

[32] R. Briggs, R. Torchio, A. Sollier, F. Occelli, L. Videau, N. Kretzschmar, and M. Wulff, "Observation of the shock-induced β-Sn to b.c.t.-Sn transition using time-resolved X-ray diffraction," Journal of Synchrotron Radiation **26**, 96–101 (2019).

[33] D. B. Bober, J. Lind, A. M. Saunders, and M. C. Akin, "X-ray diffraction from shock driven Sn microjets," Journal of Applied Physics **132** (2022), 10.1063/5.0111216.

[34] D. V. Morgan, M. Grover, D. Macy, M. Madlener, G. Stevens, and W. D. Turley, "Observations of shock-loaded tin and zirconium surfaces with single-pulse X-ray diffraction," Powder Diffraction **25**, 138–142 (2010).

[35] F. Wu, X. Li, Z. Duan, Y. Wang, Y. Gan, Y. Sun, Y. Wang, S. Chen, H. Geng, Y. Yu, and J. Hu, "Double-shock induced spall damage and recompression in tin: experimental and modeling insights into dynamic damage evolution," International Journal of Impact Engineering **210** (2026), 10.1016/j.ijimpeng.2025.105595.

[36] D. B. Holtkamp, D. A. Clark, E. N. Ferm, R. A. Gallegos, D. Hammon, W. F. Hemsing, G. E. Hogan, V. H. Holmes, N. S. P. King, R. Liljestrand, R. P. Lopez, F. E. Merrill, C. L. Morris, K. B. Morley, M. M. Murray, P. D. Pazuchanics, K. P. Prestridge, J. P. Quintana, A. Saunders, T. Schafer, M. A. Shinas, and H. L. Stacy, "A survey of high explosive-induced damage and spall in selected metals using proton radiography," in *Shock Compression of Condensed Matter - 2003* (AIP Publishing, 2004) pp. 477–482.

[37] G. I. Kanel, A. S. Savinykh, G. V. Garkushin, and S. V. Razorenov, "Dynamic strength of tin and lead melts," JETP Letters **102**, 548–551 (2015).

[38] S. I. Ashitkov, P. S. Komarov, A. V. Ovchinnikov, E. V. Struleva, and M. B. Agranat, "Strength of liquid tin at extremely high strain rates under a femtosecond laser action," JETP Letters **103**, 544–548 (2016).

[39] T. Chong, J. Mo, H. Fu, T. Li, and B. Luo, "Phase transition and spall behavior of tin under ramp wave compression," Lixue Xuebao/Chinese Journal of Theoretical and Applied Mechanics **55**, 113–119 (2023).

[40] T. de Rességuier, L. Signor, A. Dragon, P. Severin, and M. Boustie, "Transition from solid to liquid spall in tin under laser shocks of increasing intensity," in *Shock Compression of Condensed Matter-2007*, Vol. 955 (2007) pp. 509–512.

[41] T. de Rességuier, L. Signor, A. Dragon, P. Severin, and M. Boustie, "Spallation in laser shock-loaded tin below and just above melting on release," Journal of Applied Physics **102** (2007), 10.1063/1.2795436.

[42] T. de Rességuier, L. Signor, A. Dragon, and G. Roy, "Dynamic fragmentation of laser shock-melted tin: Experiment and modelling," International Journal of Fracture **163**, 109–119 (2010).

[43] T. D. Rességuier, E. Lescoute, A. Sollier, G. Prudhomme, and P. Mercier, "Microjetting from grooved surfaces in metallic samples subjected to laser driven shocks," Journal of Applied Physics **115** (2014), 10.1063/1.4863719.

[44] J. Yang, X. Wang, L. Xu, Q. Wang, Y. Sun, J. Li, L. Zhang, Y. Li, Y. Yu, P. Wang, Q. Wu, and J. Hu, "Direct visualization of laser-driven dynamic fragmentation in tin by in situ x-ray diffraction," Matter and Radiation at Extremes **9**, 057803 (2024), https://pubs.aip.org/aip/mre/article-pdf/doi/10.1063/5.0200242/20269202/057803_1_5.0200242.pdf.

[45] X. Yang, H. Zhao, X. Gao, Z. Chen, X. Zeng, and F. Wang, "Molecular dynamics study on spallation fracture in single crystal and nanocrystalline tin," Journal of Applied Physics **132** (2022), 10.1063/5.0099331.

[46] X. X. Wang, A. M. He, T. T. Zhou, and P. Wang, "Spall damage in single crystal tin under shock wave loading: A molecular dynamics simulation,"

Mechanics of Materials **160** (2021), 10.1016/j.mechmat.2021.103991.

[47] Y. Liao, M. Xiang, X. Zeng, and J. Chen, "Molecular dynamics study of the micro-spallation of single crystal tin," Computational Materials Science **95**, 89–98 (2014).

[48] F. Q. Zhao, T. T. Zhou, A. He, and P. Wang, "A coupling model of melting and damage evolution in the spallation of tin under shock loading," Journal of Applied Physics **138** (2025), 10.1063/5.0284666.

[49] X. Liang, J. G. Threadingham, E. Leggett, L. C. Smith, R. Paddock, M. D. Fitzgerald, A. Rack, D. J. Chapman, and D. E. Eakins, "Nanosecond timescale measurement of damage evolution in shock compressed magnesium alloy," (2026), in preparation.

[50] J. G. Threadingham, X. Liang, J. C. F. Millett, G. Whiteman, D. J. Chapman, and D. E. Eakins, "Demonstration of a telecentric lens relay system for PDV in plate-impact experiments," in *23rd Biennial Conference of the APS Topical Group on Shock Compression of Condensed Matter*, Vol. 3066 (2024) p. 450015.

[51] W. W. Anderson, F. Cverna, R. S. Hixson, J. Vorthman, M. D. Wilke, G. T. I. Gray, and K. L. Brown, "Phase transition and spall behavior in β-tin," in *Shock Compression of Condensed Matter - 1999* (AIP Publishing, 2000) pp. 443–446.

[52] S. P. Marsh, "LASL shock Hugoniot data," Tech. Rep. (1980).

[53] C. Mabire, *Transformation polymorphique et fusion de l'étain sous choc dans la gamme 0-100 GPa; étude expérimentale et modélisation*, Ph.D. thesis, Université de Poitiers (1999).

[54] C. Mabire and P. L. Héreil, "Shock induced polymorphic transition and melting of tin," in *Shock Compression of Condensed Matter - 1999*, Vol. 505 (AIP Publishing, 2000) pp. 93–96.

[55] M. B. Gitis and I. G. Mikhailov, "Propagation of sound in liquid metals (review)," Soviet Physics-Acoustics **12**, 131–143 (1966).

[56] K. D. Swartz, W. B. Chua, and C. Elbaum, "Third-order elastic constants of tin and of a tin-indium alloy," Physical Review B **6**, 426–435 (1972).

[57] T. Antoun, L. Seaman, D. R. Curran, G. I. Kanel, S. V. Razorenov, and A. V. Utkin, *Spall Fracture* (Springer-Verlag, 2003).

[58] G. I. Kanel, S. V. Razorenov, and V. E. Fortov, "Kinetics of spallation rupture in the aluminum alloy AMg6M," Journal of Applied Mechanics and Technical Physics **25**, 707–711 (1984).

[59] V. D. Gluzman and G. I. Kanel, "Measurement of the tensile stresses behind a spalling plane," Journal of Applied Mechanics and Technical Physics **24**, 582–585 (1983).

[60] V. I. Romanchenko and G. V. Stepanov, "Dependence of the critical stresses on the loading time parameters during spall in copper, aluminum, and steel," Journal of Applied Mechanics and Technical Physics **21**, 555–561 (1980).

[61] V. Romanchenko, "Measurement of material strength characteristics with shock-wave loading by "artificial" spalling," Strength of Materials **15**, 206–209 (1983).

[62] A. N. Dremin and A. M. Molodets, "Kinetic characteristics of spall fracture," Journal of Applied Mechanics and Technical Physics **21**, 806–813 (1980).

[63] J. R. Kreer, "Dynamic fracture in 6061-T6 aluminum," Tech. Rep. (Air Force Weapons Laboratory, 1971).

[64] J. H. Smith, "Three low-pressure spall thresholds in copper," Tech. Rep. (Sandia Corporation, 1963).

[65] W. D. Turley, S. J. Fensin, R. S. Hixson, D. R. Jones, B. M. L. Lone, G. D. Stevens, S. A. Thomas, and L. R. Veeser, "Spall response of single-crystal copper," Journal of Applied Physics **123** (2018), 10.1063/1.5012267.

[66] A. V. Utkin, "Effect of initial failure rate of the formation of a spalling pulse," Journal of Applied Mechanics and Technical Physics **34**, 578–584 (1993).

[67] D. J. Steinberg, "Equation of state and strength properties of selected materials," Tech. Rep. (1996).

[68] J. M. Walsh, M. H. Rice, R. G. Mcqueen, and F. L. Yarger, "Shock-wave compressions of twenty-seven metals. Equations of state of metals," Physical Review **108** (1957), 10.1103/PhysRev.108.196.

[69] D. Grady, *Physics of Shock and Impact*, Vol. 1 (IOP Publishing, 2017).

[70] J. Buchar, S. Rolc, J. Pecháček, and J. Krejčí, "Behaviour of uranium alloys at high loading rates," Journal de Physique IV Proceedings **1**, 197–202 (1991).

[71] D. E. Grady, "Metallurgical applications of shock-wave and high-strain-rate phenomena," (Taylor & Francis, 1986) Chap. Steady-wave risetime and spall measurements on uranium (3-15GPa), pp. 763–780.

[72] C. Wiesner and H. MacGillivray, "Fracture, plastic flow and structural integrity," (CRC Press, 2019) Chap. Loading Rate Effects on Tensile Properties and Fracture Toughness of Steel, pp. 149–174.

[73] A. Nourani and J. K. Spelt, "Effect of processing parameters on fracture toughness of lead-free solder joints," Engineering Fracture Mechanics **142**, 64–78 (2015).

[74] K. H. Prakash and T. Sritharan, "Tensile fracture of tin-lead solder joints in copper," Materials Science and Engineering: A **379**, 277–285 (2004).

[75] J. Obinata and E. Schmid, "Über die dehnung von zinnkristallen." Zeitschrift für Physik **82**, 224–234 (1933).

[76] K. Bausch, "Untersuchung der schiebegleitung an zinneinkristallen," Zeitschrift für Physik **93**, 476–509 (1935).

[77] K. Ischii, "Deformation twinning of tin single crystals under impact loading," Journal of the Physical Society of Japan **14**, 1315–1321 (1959).

[78] L. C. Tyte, "The rate of viscous flow of metals: Part 1, tin," Proceedings of the Physical Society **50**, 153–175 (1938).

[79] J. Weertman and J. E. Breen, "Creep of tin single crystals," Journal of Applied Physics **27**, 1189–1193 (1956).

[80] J. E. Breen and J. Weertman, "Creep of polycrystalline tin," Journal of Metals **7**, 1230–1234 (1955).

[81] W. Boas and P. J. Fensham, "Rate of self diffusion in tin crystals," Nature **164**, 1127–1128 (1941).

[82] R. E. Frenkel, O. D. Sherby, and J. E. Dornt, "Activation energies for creep of cadmium, indium, and tin," Acta Metallurgica **3**, 470–472 (1955).

[83] V. Raman and R. Berriche, "An investigation of the creep processes in tin and aluminum using a depth-sensing indentation technique," Journal of Materials Research **7**, 627–638 (1992).

[84] F. A. Mohamed, K. L. Murty, and J. W. Morris, "Harper-dorn creep in Al, Pb, and Sn," Metallurgical Transactions **4**, 935–940 (1973).

[85] N. A. Smirnov, "Ab initio calculations of the phase diagrams of tin and lead under pressures up to a few TPa," Journal of Physics Condensed Matter **33** (2021), 10.1088/1361-648X/abbbc5.